Advanced Functional Materials

ADVANCED FUNCTIONAL MATERIALS
www.afm-journal.de

RESEARCH ARTICLE OPEN ACCESS

Bio-Derived Polyelectrolyte Additive–Induced Interfacial Ion-Diffusion Barriers for Nonvolatile Organic Artificial Synapses

Chaeyeon Han[1] | Donghwa Lee[1] | Hyeonse Kim[1] | Hyoik Jang[1] | Sein Chung[2] | Geun Yeol Bae[3] | Eunho Lee[1]

[1]Department of Chemical and Biomolecular Engineering, Seoul National University of Science and Technology, Seoul, Republic of Korea | [2]Department of Chemical Engineering, Pohang University of Science and Technology, Pohang, Republic of Korea | [3]Department of Materials Design Engineering, Kumoh National Institute of Technology, Gumi, Republic of Korea

Correspondence: Eunho Lee (ehl@seoultech.ac.kr)

Received: 19 March 2026 | **Revised:** 28 May 2026 | **Accepted:** 13 July 2026

Keywords: artificial synapse | bio-derived additive | ion-diffusion barrier | ion dynamics | nonvolatile

ABSTRACT

Organic electrochemical synaptic transistors (OESTs) are promising neuromorphic platforms, yet their nonvolatile operation is fundamentally limited by rapid ion back-diffusion governed by interfacial ion relaxation at the electrolyte–semiconductor boundary. Channel-level optimization alone cannot prevent post-bias ion relaxation driven by concentration gradients in the electrolyte. In this context, polymer additives offer an effective route to regulate interfacial ion transport without modifying the semiconductor channel. Here, bio-derived sodium alginate is incorporated into a Na–TFSI electrolyte to reconstruct the electrolyte/channel interface and modulate ion redistribution. The resulting interfacial ion-trapping barrier suppresses back-diffusion and prolongs relaxation times of doped ions. This electrolyte-level control markedly enhances synaptic retention and improves linearity and dynamic range in long-term potentiation/depression (LTP/D) characteristics. These findings establish interfacial ion regulation at the electrolyte level as a decisive design principle for organic neuromorphic systems and highlight naturally derived polyelectrolytes as promising additives for stable synaptic operation.

1 | Introduction

Organic electrochemical synaptic transistors (OESTs) have emerged as promising platform for next-generation neuromorphic devices owing to their high conductivity, biocompatibility, and excellent mechanical flexibility [1–7]. In OESTs, electrolyte ions migrate into the organic semiconductor channel, where their accumulation modulates channel conductance to emulate synaptic weight states. However, achieving nonvolatile synaptic behavior, which is essential for stable memory retention in neuromorphic systems, remains challenging in OEST-based devices due to unstable ion transport [8, 9]. When the external bias is removed, doped ions rapidly back-diffuse into the electrolyte under concentration gradients and interfacial electrochemical driving forces. This rapid ion back-diffusion destabilizes the programmed ionic distribution and compromises long-term memory retention [10]. To address these limitations, channel-centric strategies based on molecular-level tuning of organic semiconductors have been proposed. These strategies have improved nonvolatile synaptic properties through various polymer interface controls, including the backbone and side chains [8, 11–14]. Among various organic semiconductors, thiophene-based

Chaeyeon Han and Donghwa Lee contributed equally to this work.

polymers have been widely adopted as channel materials in OECTs owing to their excellent electrochemical stability and tunable ion permeability enabled by glycol side chains [15, 16]. Specifically, high charge carrier mobility has been reported to effectively enhance ion doping characteristics [16, 17]. Although these strategies enhance doping efficiency during ion injection, the depth of ion penetration and the stability of the doped state are ultimately dictated by electrolyte-controlled ion transport. In particular, fixed channel structures impose intrinsic constraints on non-volatile operation, owing to the difficulty in actively controlling long-term ion retention and interfacial trapping behavior.

In this context, electrolyte design emerges as a key determinant of ion back-diffusion after bias removal. Controlling electrolyte composition has attracted increasing interest because it enables modulation of ion dynamics without altering the structure of organic semiconductor channels [18, 19]. However, in most electrolyte systems, interfacial ions rapidly back-diffuse into the electrolyte as the electric double layer (EDL) depolarizes [20, 15]. This reflects the absence of effective physical or kinetic barriers at the electrolyte/channel interface to stabilize the doped ionic state. Unlike the structurally fixed semiconductor channel, the electrolyte represents a dynamically reconfigurable medium in which ion transport and interfacial interactions can be tailored. From this perspective, polymer matrix–based functional additives have been proposed to localize ion transport and promote stable interfacial ion retention [21]. Specifically, polymer additives can potentially regulate interfacial ion diffusion pathways while preserving the intrinsic ion transport characteristics of the electrolyte. However, the relationship between the physicochemical properties of electrolyte additives and the resulting synaptic device characteristics remains insufficiently understood. In particular, how additive-induced interionic interactions and interfacial ion redistribution influence ion retention and back-diffusion in synaptic transistors has not been clearly established. Therefore, establishing a clear correlation between electrolyte additive properties and synaptic device behavior is criticall needed.

Here, we introduce bio-derived sodium alginate (SA) into the [Na-TFSI] electrolyte and systematically investigate its impact on ion transport and synaptic retention in OESTs. The abundant hydroxyl and carboxyl functional groups in SA enable electrostatic interactions with mobile ions, reshaping interfacial ion distribution and relaxation dynamics. These interactions establish effective interfacial barriers that suppress rapid ion back-diffusion and stabilize the doped ionic state. Comprehensive physicochemical and electrochemical analyses were conducted to elucidate the underlying mechanism of ion regulation. The incorporation of SA facilitates efficient ion penetration during programming while stabilizing ion retention during relaxation. This control over ion dynamics leads to enhanced nonvolatile retention, reliable paired-pulse facilitation (PPF), and improved linearity and dynamic range in long-term potentiation/depression (LTP/D) characteristics. Artificial neural network (ANN) simulations based on these stabilized synaptic responses achieve high learning accuracy. Collectively, these findings establish a direct electrolyte–ion transport–synaptic function relationship and define electrolyte-level regulation as a decisive design parameter for organic neuromorphic systems.

2 | Results and Discussion

Figure 1a presents a schematic illustration of biological synapses and OESTs mimicking their operating principles. A biological synapse consists of a presynaptic neuron, a postsynaptic neuron, and a synaptic cleft. When a biological pulse reaches the presynaptic neuron, neurotransmitters diffuse across the synaptic cleft to the postsynaptic neuron. This process is regulated by synaptic weights, resulting in increased or decreased neurotransmitter transport [22, 23]. Inspired by this mechanism, OESTs emulate synaptic signal transmission by controlling ion migration within the electrolyte under an applied gate bias applied through an Au tip inserted directly into the electrolyte. In OESTs, the gate voltage, electrolyte, and Poly[3,3′-bis[2-[2-(2-methoxyethoxy)ethoxy]ethoxy]-2,2′:5′,2″-terthiophene-5,5″-diyl] (p(g2T-T)) channel correspond to the presynaptic neuron, neurotransmitter, and postsynaptic neuron, respectively. Upon applying a gate voltage, anions in the electrolyte migrate into the channel, with the extent of ion migration governed by the applied voltage. This process modulates the postsynaptic current (PSC), leading to its potentiation or depression [10]. To replicate this mechanism, P(g2T-T) was spin-coated onto a Si/SiO_2 substrate to form the channel layer (Figure S1). To enhance synaptic characteristics, sodium alginate (SA) was incorporated into the [Na-TFSI] electrolyte (Figure 1b). [SA] contains abundant hydroxyl and carboxyl groups, which impart polyanionic properties [24, 25]. Owing to these properties, sodium alginate migrates toward the polymer film under an applied electric field [26]. Due to its large molecular size, however, it cannot penetrate the channel bulk and instead accumulates at the electrolyte/channel interface. This interfacial accumulation facilitates ion doping at the channel surface. To verify the electrolyte mixing characteristics, Raman spectroscopy was performed (Figure 1c). In [Na-TFSI] and [SA], distinct peaks appear near 745 and 826 cm^{-1}, respectively, corresponding to $[TFSI]^-$ and sodium alginate [27–30]. In contrast, both peaks are simultaneously present in [SA][Na-TFSI], confirming the successful incorporation of [SA] into the [Na-TFSI] electrolyte. UV–Vis spectroscopy further reveals characteristic absorption peaks in both [SA] and [SA][Na-TFSI] (Figure 1d). This suggests uniform mixing within the electrolyte while maintaining the characteristics of [SA] in the mixed solution.

To evaluate the electrical characteristics of the fabricated OESTs, transfer curves were measured over a gate voltage range from +2 to −3 V (Figure S2). All devices exhibited clockwise hysteresis, originating from the diffusion of mobile ions into the channel under the applied voltage. Quantitatively, the [SA][Na-TFSI] OEST exhibited a positive shift in V_{th} from −1.54 to −1.00 V and an increase in $I_{D,\,max}$ from 0.10 to 0.32 mA, indicating that SA reduces the effective programming bias and enhances the on-current (Table S1). The enlarged hysteresis window from 0.99 to 1.75 V further indicates stronger ion-induced conductance modulation and enhanced ion retention after [SA] incorporation [21]. To further investigate synaptic characteristics, short-term plasticity (STP) was evaluated under single pulses with varying amplitudes (V_{spike} = −1.5, −1.8, −2.0, and −2.2 V) (Figure 2a,b). STP was measured using a pulse width of 60 ms and a drain voltage of −0.01 V. In all OESTs, the EPSC rapidly reached its peak upon pulse application. In both devices, the EPSC reached

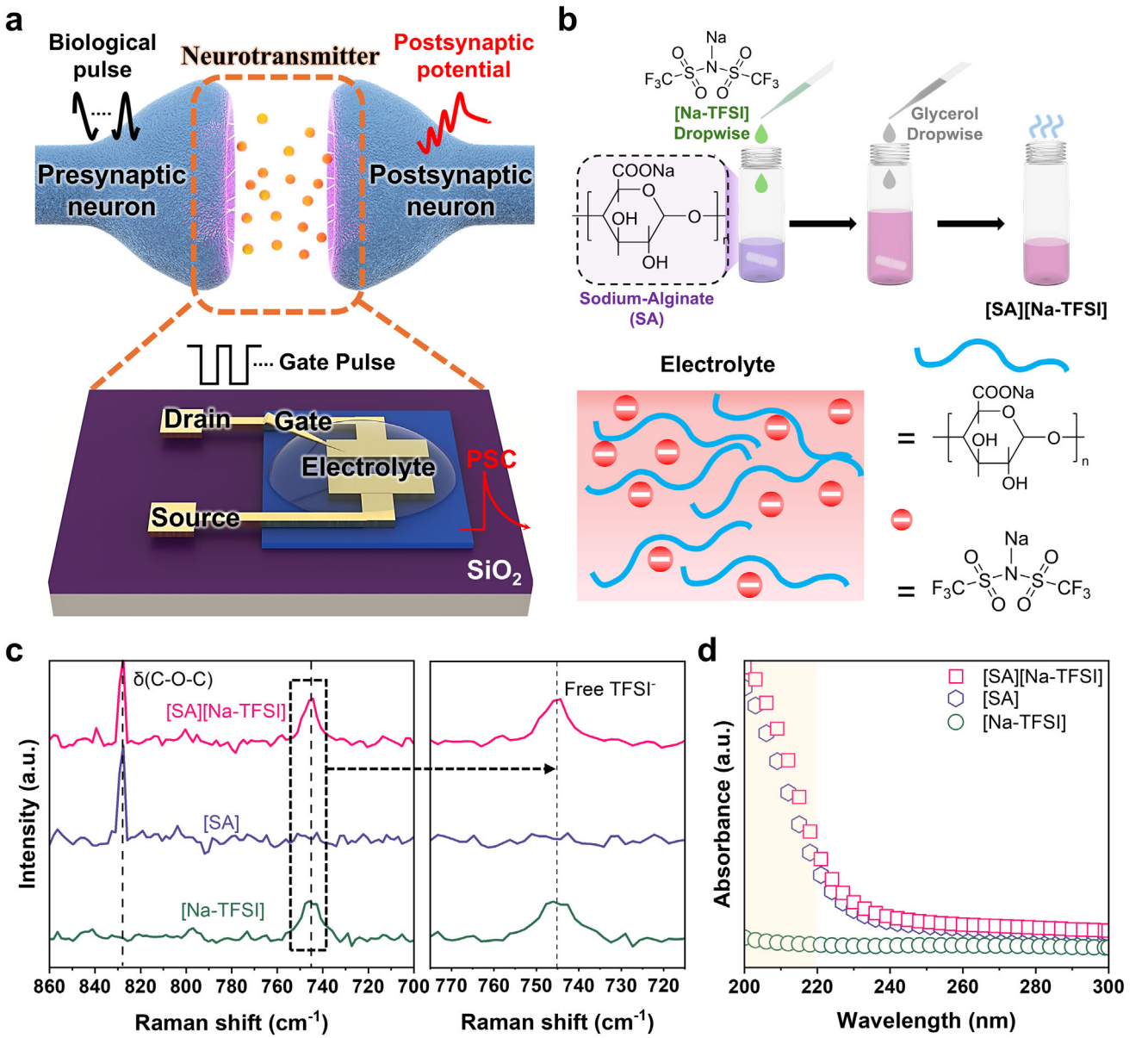

FIGURE 1 | (a) Schematic illustration of a biological synapse transmitting signals from a presynaptic neuron to a postsynaptic neuron through neurotransmitters, and an artificial synapse based on organic electrochemical synaptic transistors (OESTs) that mimic the biological synapse. (b) Synthesis procedure for the Na-TFSI-based sodium alginate electrolyte introduced into OESTs. (c) Raman and (d) UV–Vis spectra of [SA], [Na-TFSI], and [SA][Na-TFSI] to evaluate electrolyte interactions.

its peak within the 60 ms programming pulse, indicating that SA incorporation does not slow the switching response. In the [Na-TFSI] OEST, the EPSC quickly returned to its initial level after pulse removal, whereas the [SA][Na-TFSI] OEST exhibited pronounced EPSC retention. Additionally, PPF was investigated at time intervals (Δt) ranging from 60 to 2500 ms (Figure S3). PPF refers to the enhancement of the second EPSC relative to the first under two consecutive pulses (Figure 2c). The PPF index, defined as A_2/A_1, (where A_1 and A_2 are the first and second EPSC peaks, respectively), was used to quantify this behavior [31, 32]. The [SA][Na-TFSI] OEST exhibited a higher PPF index than that of the [Na-TFSI] at all time intervals, while the PPF index decreased with increasing interval (Figure 2d). The PPF index was fitted using a double exponential equation [33–35].

$$PPF = C_0 + C_1 \exp\left(-\frac{\Delta t}{\tau_1}\right) + C_2 \exp\left(-\frac{\Delta t}{\tau_2}\right) \quad (1)$$

where C_0, C_1, and C_2 represent the facilitation magnitudes. Δt is the time interval between two consecutive pulses, and τ_1 and τ_2 are the relaxation times of each phase. The parameters extracted from the [Na-TFSI] OEST were $C_0 = 0.998$, $\tau_1 = 37.81$ ms, and $\tau_2 = 648.46$ ms, while the [SA][Na-TFSI] OEST exhibited $C_0 = 1.271$, $\tau_1 = 84.44$ ms, and $\tau_2 = 1640.59$ ms. Furthermore, the [SA][Na-TFSI] OEST showed larger τ_1 and τ_2 values than those of the [Na-TFSI] OEST, indicating enhanced synaptic plasticity. The

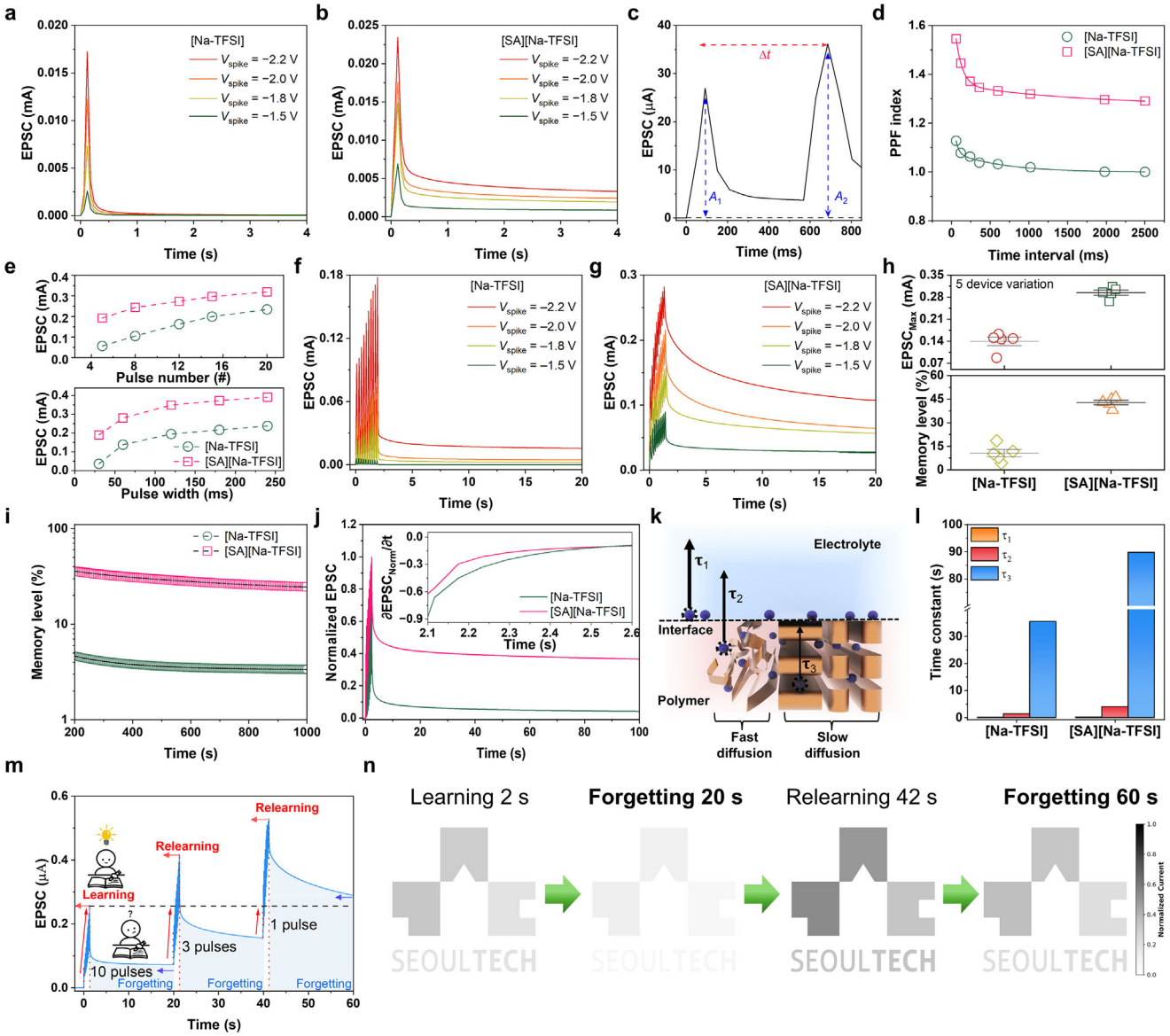

FIGURE 2 | Analysis of non-volatile characteristics of OESTs. Short-term plasticity (STP) characteristics of (a) [Na-TFSI] and (b) [SA][Na-TFSI] OESTs. A single pulse was applied at four different amplitudes (−1.5, −1.8, −2.0, and −2.2 V). (c) EPSC response triggered by two consecutive pulses applied to [SA][Na-TFSI] OESTs with a 600 ms pulse interval. (d) Paired-pulse facilitation (PPF) index based on the interval between two consecutive pulses, measured over intervals ranging from 60 to 2500 ms. (e) Maximum EPSC responses of [Na-TFSI] and [SA][Na-TFSI] OESTs as a function of pulse width and pulse number. EPSC responses of (f) [Na-TFSI] and (g) [SA][Na-TFSI] OESTs under 10 consecutive pulses applied at four different amplitudes (−1.5, −1.8, −2.0, and −2.2 V). (h) Maximum EPSC ($EPSC_{max}$) and memory level (%) of [Na-TFSI] and [SA][Na-TFSI] OESTs across five devices. (i) Memory level (%) of [Na-TFSI] and [SA][Na-TFSI] OESTs up to 1000 s. (j) Normalized EPSC curves for [Na-TFSI] and [SA][Na-TFSI] OESTs. Inset: First derivative of the normalized EPSC curve. (k) Schematic illustration of the ion diffusion process after pulse removal in the electric double layer, amorphous, and crystalline domains. l) Relaxation time constants (τ_1, τ_2, and τ_3) calculated from the tri-exponential decay function. (m) "Learning–Forgetting" behavior induced by applying 10 identical consecutive pulses to [SA][Na-TFSI] OESTs. (n) Demonstration of learning–forgetting behavior obtained from normalized current.

increased τ_1 and τ_2 values in the [SA][Na-TFSI] OEST indicate that SA prolongs the residual ionic state between consecutive pulses, thereby enhancing PPF behavior and short-term synaptic facilitation. Subsequently, to analyze the non-volatile synaptic characteristics, EPSC changes were examined as a function of pulse number and pulse width (Figure S4). In both [SA][Na-TFSI] and [Na-TFSI] OESTs, the EPSC increased with increasing pulse number and width (Figure 2e), indicating progressive ion accumulation within the channel. This behavior suggests that $[TFSI]^-$ ion migration under repeated stimulation enhances synaptic plasticity and nonvolatile characteristics. To further assess nonvolatile memory performance, 10 consecutive pulses with varying amplitudes (V_{spike} = −1.5, −1.8, −2.0, and −2.2 V) were applied (Figure 2f,g) [36]. Both the pulse width and pulse interval were fixed at 60 ms. After 10 consecutive pulses, the [Na-TFSI] OEST rapidly returned to its initial state, whereas the [SA][Na-TFSI] OEST retained an EPSC under all amplitude conditions, demonstrating enhanced retention behavior. To

quantitatively evaluate non-volatile properties, the maximum EPSC ($EPSC_{max}$) and memory level were extracted (Figure 2h). The memory level was defined as the ratio of the EPSC measured after 20 s to the maximum EPSC ($EPSC_{20\,s}/EPSC_{max}$). The [SA][Na-TFSI] OEST exhibited higher $EPSC_{max}$ and memory levels than the [Na-TFSI] OEST, and this trend is consistently observed across five devices (Figure S5). Additionally, to confirm the temporal scalability of EPSC responses, the memory level was monitored up to 1000 s (Figure 2i). The [SA][Na-TFSI] OEST exhibited a memory level of 24.5%, approximately seven times higher than that of the [Na-TFSI] OEST (3.37%), demonstrating significantly improved non-volatile synaptic characteristics. The nonvolatile retention performance of the [SA][Na-TFSI] OEST was further benchmarked with representative OECT/OEST-based synaptic devices (Table S2). To analyze the diffusion kinetics of doped anions, the first derivative of the normalized EPSC was evaluated (Figure 2j). The [SA][Na-TFSI] OEST showed a shorter transient response than the [Na-TFSI] OEST, indicating suppressed back-diffusion and prolonged ion retention at the electrolyte/channel interface. To investigate the nonvolatile characteristics of the doped ions, a tri-exponential model was employed to describe their dynamics within the channel layer (Figure S6) [37, 38].

$$I_{D,\,\mathrm{norm}} = I_{100,\,\mathrm{norm}} + A_1 \exp\left(\frac{-(t-t_0)}{\tau_1}\right) + A_2 \exp\left(\frac{-(t-t_0)}{\tau_2}\right) + A_3 \exp\left(\frac{-(t-t_0)}{\tau_3}\right) \quad (2)$$

where $I_{100,\,\mathrm{norm}}$ is the normalized EPSC measured after 100 s, and A_1, A_2, and A_3 are EPSC pre-factors. t represents time, t_0 denotes the end time of the last pulse, and τ_1, τ_2, and τ_3 are relaxation times. τ_1 corresponds to depolarization at the electrolyte/polymer interface, while τ_2 indicates the rapid back-diffusion of doped anions. The τ_3, a key parameter determining non-volatile retention characteristics, denotes the slow back-diffusion of doped anions (Figure 2k) [39]. The [SA][Na-TFSI] OEST exhibited higher time constants than the [Na-TFSI] OEST under all conditions (Figure 2l). In particular, the τ_3 extracted from the [SA][Na-TFSI] OEST was 89.8 s, which is significantly longer than that of the [Na-TFSI] OEST (35.5 s). This suggests that [SA][Na-TFSI] OEST exhibits long-term retention characteristics and effectively suppresses the back-diffusion of anions.

The [SA][Na-TFSI] OEST enables the emulation of a psychological model for human learning and memory [40]. To systematically mimic brain functions such as learning, forgetting, and memory, 10 identical pulses were applied to the [SA][Na-TFSI] OEST. The learning–forgetting process was constructed by applying pulses with fixed time intervals in an alternating manner (Figure 2m). Learning, forgetting, and relearning were sequentially implemented. The increase in current upon pulse application is defined as the learning stage, whereas the decay after pulse removal corresponds to the forgetting stage [41]. During relearning, three pulses were sufficient to reach the maximum EPSC of the initial learning stage, while only a single pulse was required in the second relearning cycle. The reduced number of required pulses highlights the enhanced learning efficiency and stable memory retention of the [SA][Na-TFSI] OEST [42]. Moreover, the EPSC peak progressively increased over repeated cycles, indicating cumulative learning behavior. The learning–forgetting process was visually analyzed using normalized current values (Figure 2n). The current values measured in the experiment were normalized with $I_{max} = 1$ and $I_{min} = 0$. Thus, the normalized current was defined as $I_{norm} = I$. In the visualization process, the normalized current values were directly applied to the image projection. After 20 s of forgetting, the normalized current decreased from 0.25 to 0.072, resulting in a blurry icon that was difficult to identify. However, after 42 s of relearning, the value increased to 0.52, resulting in a much clearer icons than before. Moreover, it maintained a value of 0.29 even after a longer forgetting process of 60 s, resulting in a relatively clear icon. These results demonstrate that the [SA][Na-TFSI] OEST effectively emulates human learning and memory processes, particularly by enhancing relearning efficiency. Overall, the incorporation of SA into the electrolyte enables stable nonvolatile synaptic behavior and supports the implementation of neuromorphic functions, highlighting its potential for advanced neuromorphic computing applications.

To observe structural changes induced by ion doping in the polymer films in [Na-TFSI] and [SA][Na-TFSI] OESTs, Raman spectroscopy was performed (Figure 3a,b). Ion doping was induced by applying a −2.2 V pulse for 10 s, followed by nitrogen drying. Before pulse application, characteristic Raman peaks appeared at 1400 and 1445 cm^{-1}. Upon electrochemical doping, these peaks shifted toward lower wavenumbers [43], reflecting increased backbone planarity and enhanced π-electron delocalization associated with polaron formation [44, 45]. In contrast, the [Na-TFSI] OEST showed negligible peak shift before and after pulse application, indicating the absence of stable polaron formation due to the rapid back-diffusion of anions. This suggests that the incorporation of [SA] promotes ion-polymer interactions, thereby inducing the formation of stable polaron structures.

To observe the real-time adsorption and diffusion behavior of ions within the polymer, in situ UV–Vis absorption spectroscopy was performed (Figure 3c). Electrochemical doping was induced by applying a bias to the film coated on an ITO substrate (Figure 3d,e). Upon doping, the absorbance at 555 nm decreases, while a broad absorption above 800 nm increases due to polaron formation [46]. To quantitatively compare the doping behavior, the normalized absorbance of the [Na-TFSI] and [SA][Na-TFSI] OESTs was analyzed (Figure 3f). After pulse application, the [Na-TFSI] OEST shows a moderate decrease in absorbance to 0.55 of its initial value, indicating limited ion injection into the polymer. In contrast, the [SA][Na-TFSI] device exhibits a pronounced decrease from 0.71 to 0.41, confirming enhanced electrochemical doping enabled by [SA]. Additionally, the [SA][Na-TFSI] OEST exhibits a pronounced increase in absorbance over the 750–900 nm range with increasing voltage, indicating enhanced polaron formation during electrochemical doping [47]. These UV–Vis results support that SA facilitates electrochemical doping under bias, as reflected by the stronger polaron-related absorption and enhanced conductance modulation. Importantly, the enhanced doping response is accompanied by a slower de-doping process after bias removal, suggesting that the SA-modified interfacial environment helps retain the doped ionic/polaronic state and retards ion back-diffusion into the electrolyte.

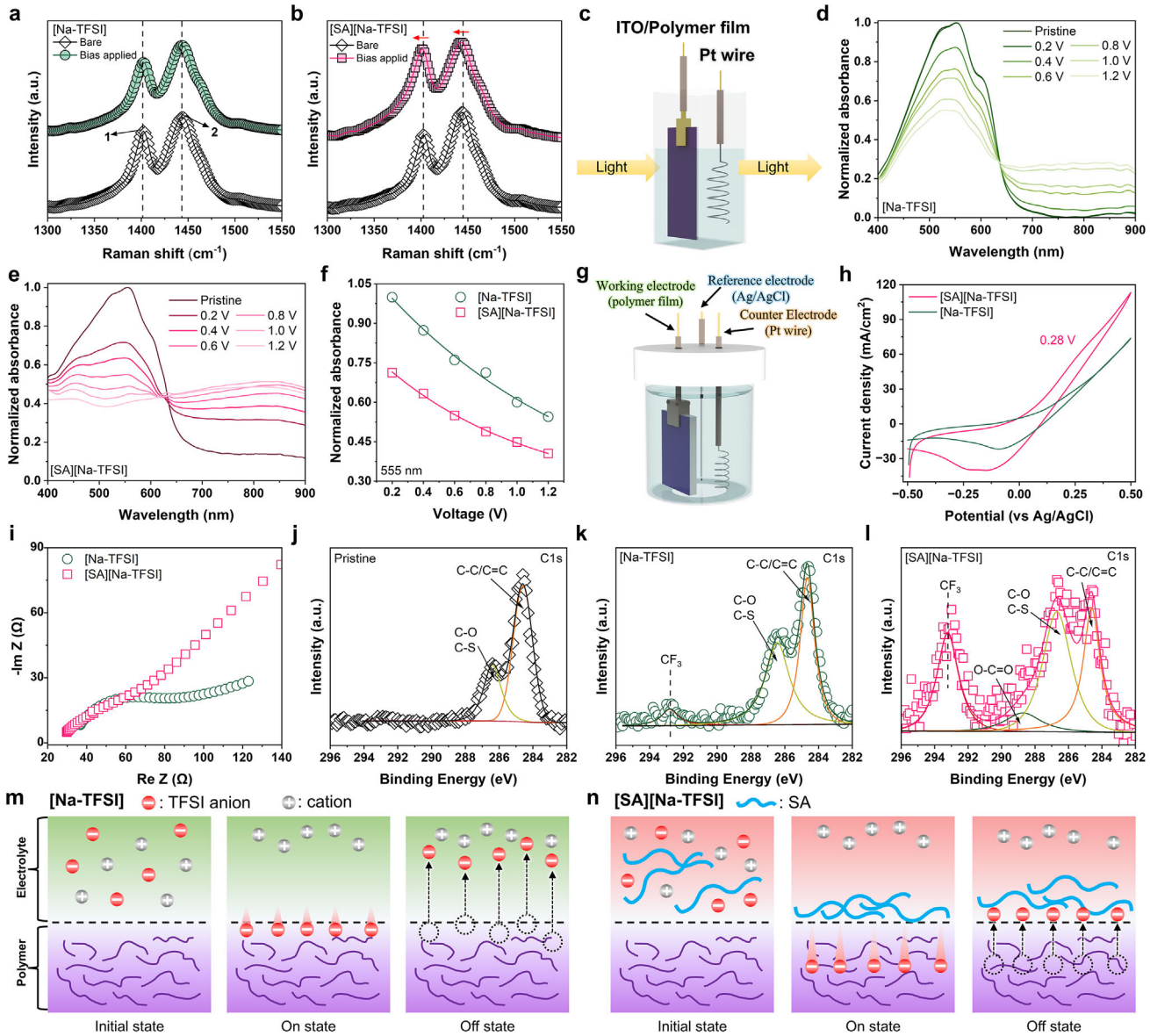

FIGURE 3 | Electrochemical doping and de-doping characteristics of [Na-TFSI] and [SA][Na-TFSI] OESTs. Raman spectra of (a) [Na-TFSI] and (b) [SA][Na-TFSI] OESTs before and after bias application. (c) Schematic illustration of the experimental setup for UV–Vis absorption spectroscopy measurements. In situ UV–Vis spectra of (d) [Na-TFSI] and (e) [SA][Na-TFSI] OESTs before pulse application and under applied voltages ranging from 0.2 V to 1.2 V. (f) Normalized absorbance of [Na-TFSI] and [SA][Na-TFSI] at a wavelength of 555 nm. (g) Schematic illustration of the experimental setup for cyclic voltammetry (CV) and electrochemical impedance spectroscopy (EIS) measurements. (h) CV measurements of [Na-TFSI] and [SA][Na-TFSI] using an Ag/AgCl reference electrode at a scan rate of 20 mV s^{-1}. (i) Nyquist plots of [Na-TFSI] and [SA][Na-TFSI] OESTs. X-ray photoelectron spectroscopy (XPS) C 1s spectra of (j) pristine, (k) [Na-TFSI] and (l) [SA][Na-TFSI] OESTs. Schematic representation of ion migration between polymers and (m) [Na-TFSI] and (n) [SA][Na-TFSI] electrolytes in response to pulses.

CV measurements were performed to investigate the interaction between the polymer film and ions. A three-electrode configuration was used with an ITO-coated polymer film as the working electrode, a Pt wire as the counter electrode, and Ag/AgCl as the reference electrode (Figure 3g). Since the polymer films coated on the ITO substrates were identical in both conditions, the differences in electrochemical behavior observed between [Na-TFSI] and [SA][Na-TFSI] are attributed to the incorporation of SA into the electrolyte. The oxidation behavior of the [Na-TFSI] and [SA][Na-TFSI] OESTs was analyzed (Figure 3h). The [SA][Na-TFSI] OEST exhibits a higher current and a distinct oxidation peak at 0.28 V, whereas the [Na-TFSI] OEST shows no clear peak within the range of −0.5 to 0.5 V. These results indicate more efficient ion injection and enhanced ion–polymer doping in the [SA][Na-TFSI] OEST. Collectively, these findings demonstrate that the incorporation of [SA] enhances electrostatic interactions under bias, promoting deeper ion penetration and improved anion doping efficiency. This efficient doping process is coupled with the subsequent stabilization of the doped ionic state by the SA-modified interfacial region after bias removal.

To further elucidate ion transport behavior at the interface and within the bulk polymer film, electrochemical impedance spectroscopy (EIS) measurements were performed. Figure 3i presents the Nyquist plots of the [Na-TFSI] and [SA][Na-TFSI] OESTs. Nyquist plots show a semicircle in the high-frequency region and a Warburg impedance in the low-frequency region [48–50]. The semicircle diameter reflects interfacial charge transfer resistance at the polymer–electrolyte interface [10]. The [SA][Na-TFSI] OEST exhibited a smaller semicircle diameter than the [Na-TFSI] OEST, indicating facilitated ion transport across the interface. This reduced interfacial resistance indicates that [SA] does not simply impede ion motion in the electrolyte, but instead promotes ion injection and charge transfer at the electrolyte/channel interface. The coexistence of reduced interfacial resistance and enhanced Warburg behavior indicates that SA enables efficient interfacial ion transfer during bias application while restricting long-range ion diffusion and post-bias relaxation within the polymer channel. Therefore, the SA-modified interfacial region serves as an ion-diffusion barrier, retarding the back-diffusion of interfacially retained ions into the electrolyte after bias removal and stabilizing the electrochemically doped state.

To further examine ion de-doping behavior, XPS analysis was performed to track binding energy changes in the polymer film. This analysis provides chemical information on the ionic species retained in the polymer channel region adjacent to the electrolyte/channel interface after bias application and electrolyte removal. Before pulse application, the pristine film exhibited C—C/C═C and C—S/C—O peaks in the C 1s spectrum (Figure 3j) [51, 52]. After pulse application, both the [Na-TFSI] and [SA][Na-TFSI] OESTs exhibited CF_3, C—S, and O═C—O peaks (Figure 3k,l), confirming the incorporation of $[TFSI]^-$ and [SA] related species into the polymer. In particular, the [SA][Na-TFSI] OEST showed enhanced CF_3 and O═C—O peaks [53, 54], indicating that [SA] promotes the retention of $[TFSI]^-$-derived species together with [SA]-related carboxylate species near the electrolyte/channel interface. In addition, we analyzed the F 1s XPS spectrum associated with $[TFSI]^-$ (Figure S7). While no signal was detected in the pristine film, distinct peaks appeared in both OESTs after pulse application, confirming the presence of CF_3 groups originating from $[TFSI]^-$ ions [55]. The stronger $[TFSI]^-$-related chemical signatures in the [SA][Na-TFSI] OEST indicate that SA suppresses the post-bias release of interfacially retained ions back into the electrolyte. These results confirm that SA stabilizes doped ionic species in the polymer channel region adjacent to the electrolyte/channel interface, thereby contributing to the interfacial ion-retention mechanism.

Based on the previous analyses, we propose a mechanistic framework describing the role of electrolyte additives in regulating ion doping retention characteristics in OESTs (Figure 3m,n). Incorporating a polymeric additive into the electrolyte modulates ion transport pathways, thereby governing doping efficiency and retention, which are key determinants of nonvolatile memory characteristics. In the [Na-TFSI] OEST, $[TFSI]^-$ ions migrate into the polymer channel under an applied electric field, inducing electrochemical doping. However, due to the lack of effective interfacial confinement, the ions rapidly back-diffuse into the electrolyte, resulting in poor retention of the doped state. In contrast, the [SA][Na-TFSI] system exhibits fundamentally different behavior. The SA matrix, rich in negatively charged carboxyl groups [56, 57], induces electrostatic interactions that regulate ion transport pathways and promote efficient ion injection into the channel [58, 59]. This accounts for the lower effective programming voltage, higher on-current, and stronger polaron formation observed in the [SA][Na-TFSI] OEST. In this context, the proposed ion-trapping barrier is defined as a dynamic interfacial barrier formed by the polymeric SA network and carboxylate-rich environment through steric and electrostatic effects. After bias removal, this SA-modified interfacial region retards the back-diffusion of retained ions into the electrolyte. As a result, the retained ions are released more slowly, allowing the doped ionic/polaronic state to remain stabilized for a longer period. This bias-dependent dual role of SA explains the simultaneous enhancement of doping efficiency and prolongation of de-doping kinetics in the [SA][Na-TFSI] OEST.

LTP/D is a key functionality in neuromorphic applications [60]. Key parameters including G_{max}/G_{min} and nonlinearity (*NL*) critically influence the accuracy of ANN simulations [61]. To evaluate the LTP/D characteristics of [Na-TFSI] and [SA][Na-TFSI] OESTs, 50 consecutive potentiation and depression pulses were applied. Potentiation pulses (60 ms) were fixed at −2.2 V, while depression pulses (60 ms) were applied at +1.0, +1.5, and +2.0 V (Figure 4a,b). The [SA][Na-TFSI] OEST exhibited improved linearity compared to the [Na-TFSI] OEST, indicating more uniform and gradual weight updates enabled by [SA]. Furthermore, the G_{max}/G_{min} ratio and *NL* values were quantitatively extracted from the LTP/D curves of both OESTs. The G_{max}/G_{min} is the ratio of maximum to minimum conductance, and the *NL* value was extracted by fitting the normalized LTP/D curves to a nonlinear function (Figure S8). Under all conditions, the [SA][Na-TFSI] OEST exhibited a high G_{max}/G_{min} and lower *NL* values, demonstrating enhanced linearity and wider dynamic range in both the potentiation and depression processes (Figure 4c,d). Moreover, stable operation under repeated cycling is essential for practical neuromorphic applications. To evaluate device stability, 2500 consecutive pulses were applied (Figure 4e). The [SA][Na-TFSI] OEST maintained stable G_{max}/G_{min} and *NL* values throughout the entire operation (Figure 4f,g), indicating robust synaptic performance under repeated cycling. Reproducibility was further assessed across five devices under identical conditions (Figure 4h). The LTP/D curves of all [SA][Na-TFSI] OESTs exhibited consistent behavior, confirming negligible device-to-device variation and stable performance.

Finally, ANN-based simulations were performed to evaluate the neuromorphic potential of the [Na-TFSI] and [SA][Na-TFSI] OESTs. Recognition accuracy was evaluated using a multi-layer perceptron (MLP) trained on the MNIST handwritten digit dataset (28 × 28 pixels) (Figure 4i). The network consisted of 784 input neurons, 100 hidden neurons, and 10 output neurons. As shown in Figure 4j, the parallel crossbar array implemented in the simulation is presented. Characteristic parameters such as G_{max}/G_{min} and *NL*, derived from the measured LTP/D characteristics, were incorporated into the simulation model. For both OESTs, the recognition accuracy increased with epochs and converged to a stable value (Figure 4k,l). Notably, the [SA][Na-TFSI] OEST consistently exhibited higher recognition

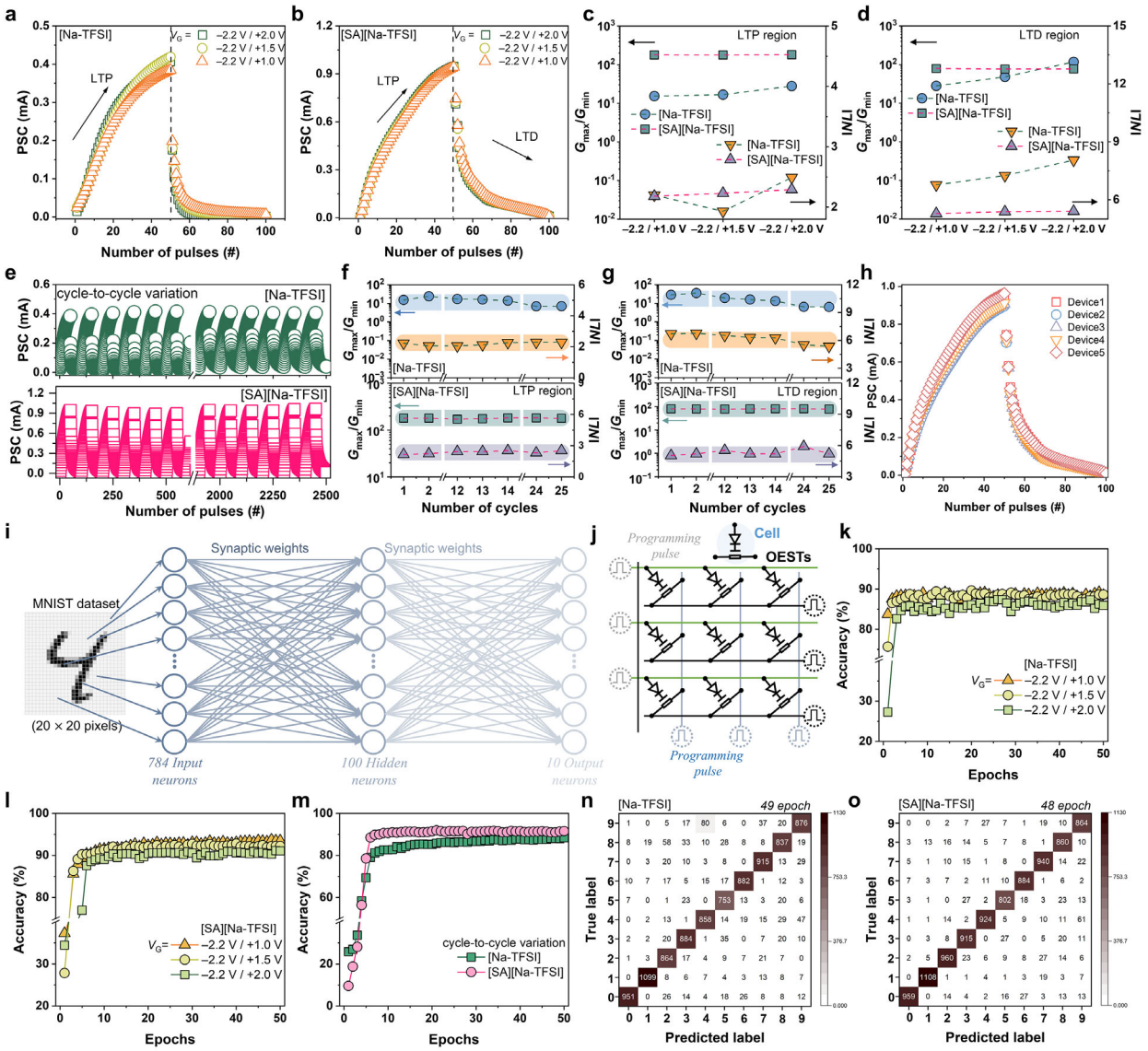

FIGURE 4 | Long-term potentiation/depression (LTP/D) operations for neural-inspired computing simulations. LTP/D responses of (a) [Na-TFSI] and (b) [SA][Na-TFSI] OESTs under 50 potentiation pulses at −2.2 V and 50 depression pulses at different amplitudes (+1.0, +1.5, and +2.0 V). *NL* and G_{max}/G_{min} derived from the (c) LTP and (d) LTD region of [Na-TFSI] and [SA][Na-TFSI] OESTs. (e) Cycle-to-cycle variations of LTP/D of [Na-TFSI] and [SA][Na-TFSI] OESTs over 25 cycles. *NL* and G_{max}/G_{min} values of the (f) LTP and (g) LTD regions extracted from 25 LTP/D cycles. (h) LTP/D characteristics of [SA][Na-TFSI] OESTs measured across five devices. MNIST simulation based on ANN for neuromorphic computing of OESTs. (i) A three-layer ANN consisting of 784 input neurons, 100 hidden neurons, and 10 output neurons. (j) Schematic illustration showing a crossbar array comprised of OESTs. Recognition accuracy for (k) [Na-TFSI] and (l) [SA][Na-TFSI] OESTs in ANN simulations with depression pulses at different amplitudes (+1.0, +1.5, and +2.0 V). (m) Recognition accuracy of [Na-TFSI] and [SA][Na-TFSI] OESTs reflecting cycle-to-cycle variation in LTP/D curves. Confusion matrices representing maximum recognition accuracy of (n) [Na-TFSI] and (o) [SA][Na-TFSI] OESTs.

accuracy across all conditions, attributed to its improved linearity and dynamic range. Under optimal conditions (−2.2 V potentiation and +1.0 V depression), the [Na-TFSI] and [SA][Na-TFSI] devices achieved maximum accuracies of 89.19% and 93.7%, respectively. Even when accounting for cycle-to-cycle variations (Figure 4m), the [SA][Na-TFSI] OEST maintained superior recognition performance, demonstrating robust and reliable synaptic behavior. Confusion matrix analysis further confirms this trend (Figure 4n,o), where the [SA][Na-TFSI] device exhibited near-ideal diagonal dominance with minimal misclassification. These results demonstrate that the incorporation of [SA] significantly enhances recognition accuracy and reliability, highlighting the potential of the [SA][Na-TFSI] OEST for advanced neuromorphic computing applications.

3 | Conclusion

In summary, this work demonstrates that nonvolatile synaptic behavior in OESTs can be effectively achieved through electrolyte-level additive design incorporating a bio-derived polymer. The introduction of SA induces electrostatic repulsion between its abundant hydroxyl and carboxyl groups and mobile ions, leading to the formation of interfacial physical barriers

within the electrolyte. These barriers regulate ion redistribution and relaxation dynamics, suppress rapid ion back-diffusion, and stabilize the electrochemical doping and dedoping processes. As a result, the devices exhibit enhanced synaptic retention, improved linearity in LTP/D characteristics, a higher Gmax/Gmin ratio, and reduced nonlinearity compared with pristine electrolyte systems. Benefiting from the stabilized weight-update behavior, ANN simulations using the MNIST dataset achieved a learning accuracy of 93.7%, reflecting the improved weight update stability. Collectively, these findings establish a direct electrolyte–ion transport–function relationship and highlight electrolyte modulation as an effective strategy for advancing neuromorphic systems.

4 | Experimental Section

4.1 | Materials and Synthesis

Poly[3,3′-bis[2-[2-(2-methoxyethoxy)ethoxy]ethoxy]-2,2′:5′,2″-terthiophene-5,5″-diyl] (P(g2T-T), M_w = 12.5 kg/mol, PDI = 2.56) was purchased from Derthon and used without further purification. Sodium bis(trifluoromethylsulfonyl)imide (Na-TFSI) was purchased from Sigma-Aldrich. Sodium alginate (SA) was purchased from Samchun Chemicals. Na-TFSI solution was prepared by completely dissolving 52.2 mg of Na-TFSI in 0.5 mL of deionized (DI) water. SA solution was prepared by gradually adding 40 mg of SA to 0.6 mL of DI water at 60°C, stirring the mixture at 350 rpm for 10 min, and then adding 0.4 mL of DI water. The prepared Na-TFSI solution was added dropwise to the SA solution, followed by additional stirring at 60°C for 20 min. Subsequently, 0.4 mL of glycerol was added dropwise. Finally, the [SA][Na-TFSI] electrolyte was obtained by evaporating water while stirring the mixture on a hot plate at 80°C for 3 h.

4.2 | Device Fabrications

Si/SiO_2 (285 nm) wafers were cut into 1.5×1.5 cm^2 pieces. These wafers were ultrasonically cleaned in isopropyl alcohol (IPA) for 20 min, rinsed with DI water, and dried with nitrogen gas. To modify the wafer surface, ultraviolet ozone treatment was performed for 5 min. A P(g2T-T) solution (4 mg mL^{-1}) was prepared by dissolving P(g2T-T) in chloroform and stirring at 50°C for 20 min. The obtained solution was filtered through a polytetrafluoroethylene (PTFE) syringe filter with a pore size of 0.45 µm. Subsequently, the channel layer was spin-coated at 1000 rpm for 60 s onto the Si/SiO_2 wafer. The gate, source, and drain electrodes were thermally evaporated as Au (40 nm) electrodes using a patterned shadow mask within a high-vacuum chamber maintained at approximately 3×10^{-5} Torr. The width and length of the defined channel are 800 and 100µm, respectively. The electrolyte was drop-cast into the channel region between the source and drain electrodes using a micropipette.

4.3 | Characterization of Synaptic Properties

To evaluate the electrical characteristics of OESTs, measurements were performed in the dark at ambient temperature using a Keithley 4200A-SCS system.

4.4 | Cyclic Voltammetry (CV) and Electrochemical Impedance Spectroscopy (EIS)

The working electrode was fabricated by spin-coating a P(g2T-T) solution onto an ITO substrate at 600 rpm for 60 s. A three-electrode system was configured using the P(g2T-T)-coated ITO as the working electrode, an Ag/AgCl reference electrode, and a Pt counter electrode. For the CV and EIS measurements, the [Na-TFSI] and [SA][Na-TFSI] electrolytes were each prepared with a total volume of 1.5 mL using the same procedure described above. The electrodes were immersed in the prepared electrolyte to perform electrochemical analysis. CV measurements were performed at a scan rate of 20 mV s^{-1} over a potential range from −0.5 to +0.5 V versus Ag/AgCl. EIS measurements were conducted using an AC amplitude of +0.1 V over a frequency range from 0.1 Hz to 1 MHz.

4.5 | In Situ UV–Vis Spectroscopy

In situ UV–vis spectroscopy was performed using a PerkinElmer Lambda 465. The P(g2T-T) solution was spin-coated onto an ITO substrate at 600 rpm for 60 s. A two-electrode system was configured using P(g2T-T)-coated ITO and a Pt wire as the working and counter electrodes, respectively.

4.6 | Simulation of Artificial Neural Network

Artificial neural network (ANN) simulations were performed on a Linux platform using NeuroSim (ver. 3.0). The simulation parameters include the number of conductance states, device-to-device and cycle-to-cycle variations, dynamic range, nonlinearity (*NL*), and pulse voltage and width.

Acknowledgements

This work was supported by the National Research Foundation of Korea (NRF) grant funded by the Ministry of Science and ICT (MSIT) (RS-2026-25490582).

Conflicts of Interest

The authors declare no conflicts of interest.

Data Availability Statement

The data that support the findings of this study are available in the supporting information of this article.

References

1. W. Huang, J. Chen, Y. Yao, et al., "Vertical Organic Electrochemical Transistors for Complementary Circuits," *Nature* 613 (2023): 496–502, https://doi.org/10.1038/s41586-022-05592-2.

2. C. M. Lee, Y. Kim, W. Kim, E. Lee, and E. K. Lee, "High-Performance Synaptic Devices Based on Cross-linked Organic Electrochemical Transistors with Dual Ion Gel," *Advanced Functional Materials* 35 (2025): 2417539, https://doi.org/10.1002/adfm.202417539.

3. D. Jeong, S. Kim, M. An, et al., "Recent Strategies in Channel Modulation for High-Performance Neuromorphic Computing Based on Electrolyte-Gated Organic Synaptic Transistors," *Korean Journal of*

Chemical Engineering 42 (2025): 2455–2466, https://doi.org/10.1007/s11814-025-00450-z.

4. D. H. Ho and J. H. Cho, "Vanishing Soft Electronics: Degradation Mechanisms of Transient Materials," *Korean Journal of Chemical Engineering* 42 (2025): 2069–2081, https://doi.org/10.1007/s11814-024-00320-0.

5. S. Lee, H. Lee, G. Jung, M. S. Kwak, Y.-R. Kim, and H. Ko, "Artificial Flexible Sensory Electronics Mimicking Human Somatosensory System," *Korean Journal of Chemical Engineering* 42 (2025): 1977–1991, https://doi.org/10.1007/s11814-024-00272-5.

6. S. Jang, Y. Kim, C. Lee, et al., "Vapor-Phase Deposited Polymer Dielectric Layers for Organic Electronics: Design, Characteristics, and Applications," *Korean Journal of Chemical Engineering* 42 (2025): 1931–1949, https://doi.org/10.1007/s11814-024-00210-5.

7. Z. Chen, X. Ding, J. Wang, X. Guo, S. Shao, and K. Feng, "π-Conjugated Polymers for High-Performance Organic Electrochemical Transistors: Molecular Design Strategies, Applications and Perspectives," *Angewandte Chemie International Edition* 64 (2025): 202423013, https://doi.org/10.1002/anie.202423013.

8. W. Shan, Y. Wang, Y. Zhong, S. Wustoni, and S. Inal, "Organic Electrochemical Synaptic Transistors with Improved Retention for Logic and Biosignal Processing," *Advanced Materials* 38 (2026): 13703, https://doi.org/10.1002/adma.202513703.

9. Y. Zhao, C. Su, G. Shen, et al., "Donor Engineering Tuning the Analog Switching Range and Operational Stability of Organic Synaptic Transistors for Neuromorphic Systems," *Advanced Functional Materials* 32 (2022): 2205744, https://doi.org/10.1002/adfm.202205744.

10. D. Lee, J. Kim, S. Chung, J. Sung, C. Han, and E. Lee, "Structure–Transport–Ion Retention Coupling for Enhanced Nonvolatile Artificial Synapses," *Advanced Functional Materials* 36 (2026): 21650, https://doi.org/10.1002/adfm.202521650.

11. J. Sung, S. Chung, Y. Jang, et al., "Unveiling the Role of Side Chain for Improving Nonvolatile Characteristics of Conjugated Polymers-Based Artificial Synapse," *Advanced Science* 11 (2024): 2400304, https://doi.org/10.1002/advs.202400304.

12. B. Wang, Y. Kong, S. Zhang, et al., "Face-on Orientation Matches Vertical Organic Electrochemical Transistors for High Transconductance and Superior Non-Volatility," *Advanced Functional Materials* 34 (2024): 2312822, https://doi.org/10.1002/adfm.202312822.

13. W. Yang, S. Ma, S. Gámez-Valenzuela, et al., "Backbone Tailoring Enables High-Performance and Stable n-Type Organic Mixed Ionic-Electronic Conductors for Synaptic Simulation and Biosensor," *Advanced Materials* 38 (2026): 12070, https://doi.org/10.1002/adma.202512070.

14. X. Zhang, R. Zhu, W. Yang, et al., "Backbone Engineering of Bithiophene Imide Dimer-Based Polymeric Mixed Ionic-Electronic Conductors for High-Performance n-Type Organic Electrochemical Transistors," *Small* 21 (2025): 2408716, https://doi.org/10.1002/smll.202408716.

15. S. Zhang, P. Ding, T.-P. Ruoko, et al., "Toward Stable p-Type Thiophene-Based Organic Electrochemical Transistors," *Advanced Functional Materials* 33 (2023): 2302249, https://doi.org/10.1002/adfm.202302249.

16. A. Savva, R. Hallani, C. Cendra, et al., "Balancing Ionic and Electronic Conduction for High-Performance Organic Electrochemical Transistors," *Advanced Functional Materials* 30 (2020): 1907657, https://doi.org/10.1002/adfm.201907657.

17. C. Zhi, J. Song, J. Chen, et al., "Emerging Gel-Based Organic Electrochemical Transistors: Device Design, Engineering, and Applications," *Advanced Functional Materials* 36 (2026): 23411, https://doi.org/10.1002/adfm.202523411.

18. H. Lee, J. Cho, M. Jin, et al., "Electrochemical Analysis of Ion Effects on Electrolyte-Gated Synaptic Transistor Characteristics," *ACS Nano* 18 (2024): 5383–5395, https://doi.org/10.1021/acsnano.3c10082.

19. W. Lee, T. Kim, H. Kim, and Y. Kim, "Controlled Migration of Lithium Cations by Diamine Bridges in Water-Processable Polymer-Based Solid-State Electrolyte Memory Layers for Organic Synaptic Transistors," *Advanced Materials* 36 (2024): 2403645, https://doi.org/10.1002/adma.202403645.

20. J. Wu, "Understanding the Electric Double-Layer Structure, Capacitance, and Charging Dynamics," *Chemical Reviews* 122 (2022): 10821–10859, https://doi.org/10.1021/acs.chemrev.2c00097.

21. D. Lee, Y. U. Jeon, M. An, et al., "Tailored Zwitterion Electrolyte-Driven Electric Double Layer Dynamics for Enhanced Ion Retention in Artificial Synapses," *Advanced Functional Materials* 36 (2026): 13684, https://doi.org/10.1002/adfm.202513684.

22. G. Liu, Q. Li, W. Shi, et al., "Ultralow-Power and Multisensory Artificial Synapse Based on Electrolyte-Gated Vertical Organic Transistors," *Advanced Functional Materials* 32 (2022): 2200959, https://doi.org/10.1002/adfm.202200959.

23. K. Hadiyal, R. Ganesan, A. Rastogi, and R. Thamankar, "Bio-inspired Artificial Synapse for Neuromorphic Computing Based on NiO Nanoparticle Thin Film," *Scientific Reports* 13 (2023): 7481, https://doi.org/10.1038/s41598-023-33752-5.

24. J. Shi, Y. Lin, Z. Wang, et al., "Adaptive Processing Enabled by Sodium Alginate Based Complementary Memristor for Neuromorphic Sensory System," *Advanced Materials* 36 (2024): 2314156, https://doi.org/10.1002/adma.202314156.

25. S. Hua, H. Ma, X. Li, H. Yang, and A. Wang, "pH-Sensitive Sodium Alginate/Poly(Vinyl Alcohol) Hydrogel Beads Prepared by Combined Ca2+ Crosslinking and Freeze-Thawing Cycles for Controlled Release of Diclofenac Sodium," *International Journal of Biological Macromolecules* 46 (2010): 517–523, https://doi.org/10.1016/j.ijbiomac.2010.03.004.

26. X. Xia, Y. Yang, X. Zhou, E. Liu, and S. Xu, "Mechanically Tunable Ion-Crosslinked Alginate-Based Gradient Hydrogels by Electrolysis-Electrophoresis Method," *Carbohydrate Polymers* 289 (2022): 119473, https://doi.org/10.1016/j.carbpol.2022.119473.

27. L. J. Hardwick, M. Holzapfel, A. Wokaun, and P. Novák, "Raman Study of lithium Coordination In EMI-TFSI Additive Systems as Lithium-Ion Battery Ionic Liquid Electrolytes," *Journal of Raman Spectroscopy* 38 (2007): 110–112, https://doi.org/10.1002/jrs.1632.

28. G. Cardenas-Jiron, D. Leal, B. Matsuhiro, and I. O. Osorio-Roman, "Vibrational Spectroscopy and Density Functional Theory Calculations of Poly- D -Mannuronate and Heteropolymeric Fractions from Sodium Alginate," *Journal of Raman Spectroscopy* 42 (2011): 870–878, https://doi.org/10.1002/jrs.2760.

29. M. M. Campos-Vallette, N. P. Chandía, E. Clavijo, et al., "Characterization of Sodium Alginate and its Block Fractions by Surface-Enhanced Raman Spectroscopy," *Journal of Raman Spectroscopy* 41 (2010): 758–763, https://doi.org/10.1002/jrs.2517.

30. Z. Zhao, F. Li, J. Zhao, et al., "Ionic-Association-Assisted Viscoelastic Nylon Electrolytes Enable Synchronously Coupled Interface for Solid Batteries," *Advanced Functional Materials* 30 (2020): 2000347, https://doi.org/10.1002/adfm.202000347.

31. T. Pan, X. Wang, J. Zhu, and H. Wang, "Preparation of Bright Yellow Color Sodium Alginate Solution," *Carbohydrate Polymers* 337 (2024): 122169, https://doi.org/10.1016/j.carbpol.2024.122169.

32. Q. Zhang, T. Jin, X. Ye, D. Geng, W. Chen, and W. Hu, "Organic Field Effect Transistor-Based Photonic Synapses: Materials, Devices, and Applications," *Advanced Functional Materials* 31 (2021): 2106151, https://doi.org/10.1002/adfm.202106151.

33. Z. Zhao, Z. Hu, M. Deng, et al., "Bias-Switchable Photodetection and Photosynapse Dual-Functional Devices Based on 2D Perovskite/Organic Heterojunction for Imaging-to-Recognition Conversion," *Advanced Materials* 37 (2025): 2416033, https://doi.org/10.1002/adma.202416033.

34. R. Yang, Y. Wang, S. Li, et al., "All-Optically Controlled Artificial Synapse Based on Full Oxides for Low-Power Visible Neural Network Computing," *Advanced Functional Materials* 34 (2024): 2312444, https://doi.org/10.1002/adfm.202312444.

35. H. Jang, H. Lee, E. Lee, and G. Y. Bae, "Nanoweb Structuring for Enhanced Ion Doping Efficiency and Long-Term Plasticity of Organic Artificial Synapses," *Chemical Engineering Journal* 525 (2025): 170501, https://doi.org/10.1016/j.cej.2025.170501.

36. X. Ji, B. D. Paulsen, G. K. K. Chik, et al., "Mimicking Associative Learning Using an Ion-Trapping Non-Volatile Synaptic Organic Electrochemical Transistor," *Nature Communications* 12 (2021): 2480, https://doi.org/10.1038/s41467-021-22680-5.F.

37. D. Lee, M. Kim, S. Park, et al., "Inter-Ion Mutual Repulsion Control for Nonvolatile Artificial Synapse," *Advanced Functional Materials* 35 (2025): 2412012, https://doi.org/10.1002/adfm.202412012.

38. D. Lee, M. Q. Li, M. An, J. Sung, J. Lee, and E. Lee, "Fundamental Control of Cation–Anion Interactions Governing Retentive Behavior in Organic Synaptic Transistor," *ACS Nano* 19 (2025): 42783–42795, https://doi.org/10.1021/acsnano.5c14187.

39. M.-J. Sung, D.-G. Seo, J. Kim, et al., "Overcoming the Trade-off Between Efficient Electrochemical Doping and High State Retention in Electrolyte-Gated Organic Synaptic Transistors," *Advanced Functional Materials* 34 (2024): 2312546, https://doi.org/10.1002/adfm.202312546.

40. H. Wan, J. Zhao, L.-W. Lo, Y. Cao, N. Sepúlveda, and C. Wang, "Multimodal Artificial Neurological Sensory–Memory System Based on Flexible Carbon Nanotube Synaptic Transistor," *ACS Nano* 15 (2021): 14587–14597, https://doi.org/10.1021/acsnano.1c04298.

41. X. Gao, D. Cui, P. Guo, et al., "Artificial Synapses and Logic Gates Based on Tellurium Oxide Memristors for Artificial Vision Applications," *Advanced Functional Materials* 36 (2026): 15165, https://doi.org/10.1002/adfm.202515165.

42. L. Wang, S. Wang, G. Xu, et al., "Ionic Potential Relaxation Effect in a Hydrogel Enabling Synapse-Like Information Processing," *ACS Nano* 18 (2024): 29704–29714, https://doi.org/10.1021/acsnano.4c09154.

43. K.-H. Choi, S. Im, A. Plant, et al., "Role of Amorphous Phases in Mixed Conduction of Conjugated Regioblock Copolymers for Organic Electrochemical Synaptic Transistors," *Advanced Materials* 37 (2025): 02133, https://doi.org/10.1002/adma.202502133.

44. P. Cavassin, I. Holzer, D. Tsokkou, O. Bardagot, J. Réhault, and N. Banerji, "Electrochemical Doping in Ordered and Disordered Domains of Organic Mixed Ionic–Electronic Conductors," *Advanced Materials* 35 (2023): 2300308, https://doi.org/10.1002/adma.202300308.

45. C. Sun, X. Liu, Q. Yao, et al., "A Discolorable Flexible Synaptic Transistor for Wearable Health Monitoring," *ACS Nano* 18 (2024): 515–525, https://doi.org/10.1021/acsnano.3c08357.

46. W. Kim, K. Lee, S. Choi, et al., "Electrochemiluminescent Tactile Visual Synapse Enabling in Situ Health Monitoring," *Nature Materials* 24 (2025): 925–934, https://doi.org/10.1038/s41563-025-02124-x.

47. P. Y. Ho, O. Ditzer, A. Solgi, et al., "Boosting OECT Performance with PEGylated Gold Nanoparticles in Hydrophobic Channels," *Advanced Functional Materials* 35 (2025): 2412559, https://doi.org/10.1002/adfm.202412559.

48. R. D. Nikam, M. Kwak, J. Lee, K. G. Rajput, W. Banerjee, and H. Hwang, "Near Ideal Synaptic Functionalities in Li Ion Synaptic Transistor Using Li3POxSex Electrolyte with High Ionic Conductivity," *Scientific Reports* 9 (2019): 18883, https://doi.org/10.1038/s41598-019-55310-8.

49. G. Wu, P. Feng, X. Wan, L. Zhu, Y. Shi, and Q. Wan, "Artificial Synaptic Devices Based on Natural Chicken Albumen Coupled Electric-Double-Layer Transistors," *Scientific Reports* 6 (2016): 23578, https://doi.org/10.1038/srep23578.

50. Y. Ko, W. Sung, and J. Ahn, "Layer-by-Layer-Structured Silicon-Based Electrode Design for Ultrafast Lithium-Ion Batteries," *Korean Journal of Chemical Engineering* 42 (2025): 1045–1053, https://doi.org/10.1007/s11814-024-00357-1.

51. J. Sung, M. Kim, S. Chung, et al., "Modulating Alkyl Groups in Copolymer to Control Ion Transport in Electrolyte-Gated Organic Transistors for Neuromorphic Computing," *Small Structures* 6 (2025): 2400319, https://doi.org/10.1002/sstr.202400319.

52. H. Jang, G. Y. Bae, S. H. Kim, J. Sung, and E. Lee, "Crosslinking-Induced Anion Transport Control for Enhancing Linearity in Organic Synaptic Devices," *Materials Horizons* 11 (2024): 4638–4650, https://doi.org/10.1039/D4MH00806E.

53. F. Hou, R. Gorthy, I. Mardon, D. Tang, and C. Goode, "Low Voltage Environmentally Friendly Plasma Electrolytic Oxidation Process for Titanium Alloys," *Scientific Reports* 12 (2022): 6037, https://doi.org/10.1038/s41598-022-09693-w.

54. Z. Mao, R. Wang, B. He, J. Jin, Y. Gong, and H. Wang, "Cross-Linked Sodium Alginate as A Multifunctional Binder to Achieve High-Rate and Long-Cycle Stability for Sodium-Ion Batteries," *Small* 19 (2023): 2207224, https://doi.org/10.1002/smll.202207224.

55. C. Chen, Q. Liang, G. Wang, D. Liu, and X. Xiong, "Grain-Boundary-Rich Artificial SEI Layer for High-Rate Lithium Metal Anodes," *Advanced Functional Materials* 32 (2022): 2107249, https://doi.org/10.1002/adfm.202107249.

56. P. Yan, W. Lan, and J. Xie, "Modification on Sodium Alginate for Food Preservation: A Review," *Trends in Food Science & Technology* 143 (2024): 104217, https://doi.org/10.1016/j.tifs.2023.104217.

57. A. Banerjee, R. De, and B. Das, "Hydrodynamic and Conformational Characterization of Aqueous Sodium Alginate Solutions with Varying Salinity," *Carbohydrate Polymers* 277 (2022): 118855, https://doi.org/10.1016/j.carbpol.2021.118855.

58. H. Guo, Q. Qin, J.-S. Chang, and D.-J. Lee, "Modified Alginate Materials for Wastewater Treatment: Application Prospects," *Bioresource Technology* 387 (2023): 129639, https://doi.org/10.1016/j.biortech.2023.129639.

59. J. Wang, Y. Huang, B. Liu, et al., "Flexible and Anti-Freezing Zinc-Ion Batteries Using a Guar-Gum/Sodium-Alginate/Ethylene-Glycol Hydrogel Electrolyte," *Energy Storage Materials* 41 (2021): 599–605, https://doi.org/10.1016/j.ensm.2021.06.034.

60. C.-S. Yang, D.-S. Shang, N. Liu, et al., "All-Solid-State Synaptic Transistor with Ultralow Conductance for Neuromorphic Computing," *Advanced Functional Materials* 28 (2018): 1804170, https://doi.org/10.1002/adfm.201804170.

61. D. Lee, J. Sung, M. Kim, et al., "Controlling Long-Term Plasticity in Neuromorphic Computing Through Modulation of Ferroelectric Polarization," *ACS Applied Materials & Interfaces* 16 (2024): 58940–58951, https://doi.org/10.1021/acsami.4c11731.

Supporting Information

Additional supporting information can be found online in the Supporting Information section.

Supporting File: adfm77301-sup-0001-SuppMat.docx.